

Dynamic ventilation imaging from four-dimensional computed tomography

This content has been downloaded from IOPscience. Please scroll down to see the full text.

2006 Phys. Med. Biol. 51 777

(<http://iopscience.iop.org/0031-9155/51/4/002>)

View [the table of contents for this issue](#), or go to the [journal homepage](#) for more

Download details:

IP Address: 128.6.218.72

This content was downloaded on 15/08/2015 at 17:21

Please note that [terms and conditions apply](#).

Dynamic ventilation imaging from four-dimensional computed tomography

Thomas Guerrero^{1,2,4}, Kevin Sanders¹, Edward Castillo², Yin Zhang²,
Luc Bidaut³, Tinsu Pan³ and Ritsuko Komaki¹

¹ Division of Radiation Oncology, The University of Texas M D Anderson Cancer Center, Houston, TX 77030-4009, USA

² Department of Computational and Applied Mathematics, Rice University, Houston, TX, USA

³ Division of Diagnostic Imaging, The University of Texas M D Anderson Cancer Center, Houston, TX, USA

E-mail: tguerrero@mdanderson.org

Received 19 July 2005, in final form 1 December 2005

Published 25 January 2006

Online at stacks.iop.org/PMB/51/777

Abstract

A novel method for dynamic ventilation imaging of the full respiratory cycle from four-dimensional computed tomography (4D CT) acquired without added contrast is presented. Three cases with 4D CT images obtained with respiratory gated acquisition for radiotherapy treatment planning were selected. Each of the 4D CT data sets was acquired during resting tidal breathing. A deformable image registration algorithm mapped each (voxel) corresponding tissue element across the 4D CT data set. From local average CT values, the change in fraction of air per voxel (i.e. local ventilation) was calculated. A 4D ventilation image set was calculated using pairs formed with the maximum expiration image volume, first the exhalation then the inhalation phases representing a complete breath cycle. A preliminary validation using manually determined lung volumes was performed. The calculated total ventilation was compared to the change in contoured lung volumes between the CT pairs (measured volume). A linear regression resulted in a slope of 1.01 and a correlation coefficient of 0.984 for the ventilation images. The spatial distribution of ventilation was found to be case specific and a 30% difference in mass-specific ventilation between the lower and upper lung halves was found. These images may be useful in radiotherapy planning.

1. Introduction

Pulmonary ventilation, the exchange of air between the lungs and the ambient air, is difficult to measure with physiologically meaningful and quantitative values in three dimensions. However, there is increasing interest in utilizing physiological images in radiotherapy treatment

⁴ Author to whom any correspondence should be addressed.

planning to avoid the irradiation of highly functional regions and minimize the loss of overall function following radiotherapy (Kwa *et al* 1995, Marks *et al* 1995, 1997, Fan *et al* 2001, Nioutsikou *et al* 2005). Currently, the volume of normal lung that will receive a specified radiation dose is utilized in radiotherapy treatment planning to estimate the risk of pulmonary injury (Graham *et al* 1999, Lee *et al* 2003). This method assumes homogeneous pulmonary function throughout the entire lung (Lyman 1985). However, patients may have significantly heterogeneous regional lung function resulting from underlying physiological differences, positioning (standing versus supine), chronic pulmonary disease or pulmonary malignancy (Altemeier *et al* 2000, Glenny *et al* 2000, Venegas and Galletti 2000). A more accurate method of risk assessment would include both the volume and the functional capacity of the portions of the lung intended for irradiation (Marks *et al* 1995, Nioutsikou *et al* 2005). An ideal method would not require radioactive tracers or special equipment and may be performed using image data already acquired as part of the treatment planning process. In this study, we develop a ventilation imaging method from four-dimensional computed tomography (4D CT) acquired for radiotherapy treatment planning that is potentially better suited and more useful for radiotherapy planning than the established methods.

Scintigraphy is the most widely used clinical imaging method to evaluate ventilation. It consists of planar projection images acquired during administration of a radioactive gas or aerosol (Alderson and Line 1980). Single photon emission computed tomography (SPECT) imaging is a more recently developed imaging method that can be used for the same purpose. Technetium Tc-99m-labelled Technegas (Burch *et al* 1986), an aerosol with a biological half-life of 135 h, provides stable distribution (Suga 2002), allowing for gated SPECT acquisition, which produces a single ventilation image. The image is determined by the distribution of radioactivity resulting from the aerosol's distribution during the single inspiration associated with its uptake. Xenon Xe-133 dynamic SPECT provides time sequence images of the washout phase after equilibration, from which regional clearance times are calculated. Ventilation SPECT imaging methods with ^{133}Xe and $^{99\text{m}}\text{Tc}$ -labelled Technegas are reviewed by Suga (2002). Positron emission tomography (PET) is another type of imaging method which uses nitrogen N-13 or neon Ne-19 for ventilation imaging (reviewed by Schuster (1998)) and may provide an improved spatial resolution over SPECT's by a factor of 2. Correlation between defects on Xe-133 SPECT imaging and differences in computed tomography (CT) values in Hounsfield units (HU) on CT images obtained at different phases of the respiratory cycle has been reported (Suga *et al* 1997).

Magnetic resonance (MR) imaging techniques for ventilation have been developed recently. With oxygen-enhanced MR imaging, images are acquired before and after a simple change in the inspiratory oxygen concentration; the subtraction images (pure oxygen breathing image minus the room air breathing image) are claimed to represent ventilation (Edelman *et al* 1996). Hyperpolarized noble gases, such as xenon Xe-129 or helium He-3, have been utilized to provide paramagnetic contrast for MR ventilation imaging (Albert *et al* 1994). MR techniques of ventilation imaging require tracer gases and specialized equipment, which may limit the availability of these methods. For example, the hyperpolarized ^3He required for contrast is not widely available, the degree of its hyperpolarization is time dependent and the resulting images reveal air space rather than ventilation. In spin-density imaging, a single inhalation of the hyperpolarized gas is followed by a breath-hold image acquisition (Altes and Salerno 2004). Other paramagnetic gases have been proposed as ventilation contrast agents, for example fluorine ^{19}F MR imaging using sulfur hexafluoride (SF_6) gas (Kuethe *et al* 2000). Asphyxiation is a danger posed by gases with a density higher than air's (e.g. Xe, SF_6). A review of MR ventilation imaging techniques can be found in Kauczor *et al* (2002).

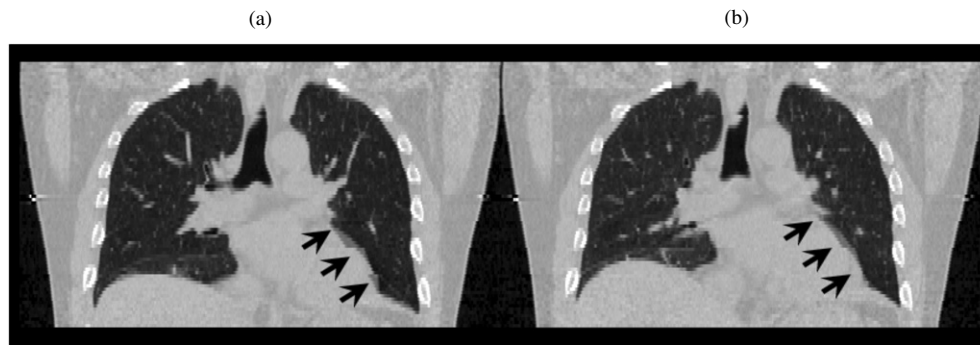


Figure 1. The 4D CT images used in this study were ten images spanning the expiratory and then inspiratory phases of an average normal resting supine breath. Coronal sections through the (a) peak inspiratory image and (b) the peak expiratory image are shown (patient 1). Note the arrows depicting the scalloped edge artefact along the lateral heart border arising due to the asynchrony between the respiratory cycle utilized for gating and the cardiac cycle.

Existing ventilation imaging techniques require a tracer gas and specialized imaging equipment such as an MR scanner or a SPECT camera, and their resulting images do not provide quantitative physiological parameters. The use of these images with CT-derived quantities, such as the radiotherapy radiation dose or tissue-density distributions, requires multimodality image registration, a potential source of error. The aerosol method is limited by settling of particles in the major airways, which confounds the resulting images. All tracer methods requiring equilibration of a tracer gas or aerosol have a shortcoming owing to backward transport from airways to cleared alveoli (Tajik *et al* 2002), differences in flow characteristics compared with air and absorption of the tracer gas into the bloodstream.

Four-dimensional CT (4D CT) imaging was developed to provide an estimate of tumour motion for radiotherapy treatment planning (Ford *et al* 2003, Vedam *et al* 2003, Pan *et al* 2004). 4D CT utilizes phase binning of images from supine patients during normal tidal breathing to acquire between 8 and 20 CT frames at phases that uniformly sample the respiratory cycle (figures 1 and 2). An external tracking device is utilized to provide a signal that corresponds with the phase of the patient's respiratory cycle. Using multislice CT scanners, either an over-sampled spiral CT or a sequentially stepped cine CT image is acquired over the entire thorax in less than 1 min (Pan 2005). Using the external signal or an internal image reference (e.g. chest wall or diaphragm), the images are sorted into bins that correspond with the phase of the respiratory cycle. The resulting image set contains up to 20 three-dimensional CT (3D CT) images with respiratory motion induced image changes across the set that are not available on a single-component 3D CT image. Within each component 3D CT image, the effects of respiratory-induced motion are minimized to a degree related to the scanner's rotation speed. The full set of images provides a view of the internal anatomical motion resulting from the respiratory cycle and has found use for tumour targeting in radiation therapy treatment planning (Mageras *et al* 2004, Underberg *et al* 2004). The resulting 4D CT image set contains respiratory-induced tumour motion as well as CT characteristics of the pulmonary parenchyma that will reflect the changes in air content.

Simon (2000) described a technique to calculate the change in the fractional content of air within pulmonary tissue between matched regions using a pair of breath-hold CT images (BH-CT), one at expiration (eBH-CT) and one at inspiration (iBH-CT). That technique, however,

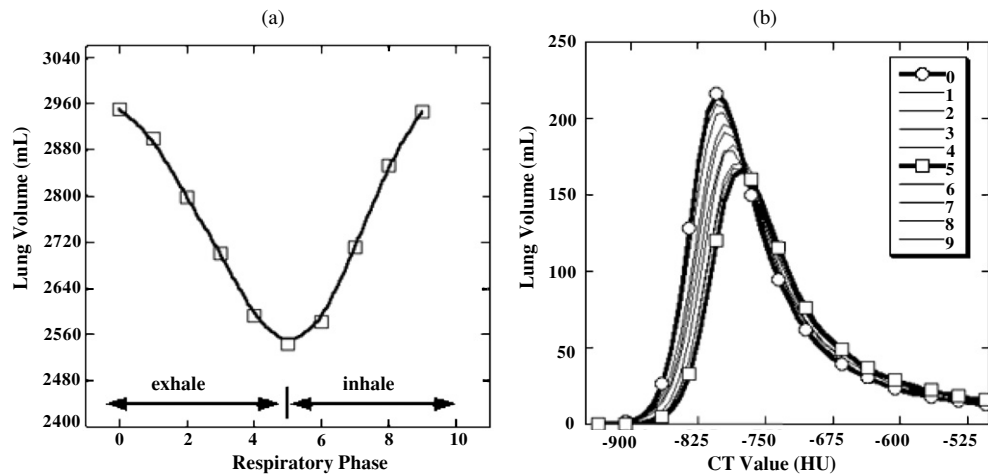


Figure 2. Pulmonary characteristics on 4D CT. (a) The bilateral lung volumes were manually delineated and the volume per image was recorded. The volume versus image phase number is shown in the graph for patient 2. (b) Histograms of the lung parenchyma CT values were obtained for each image. Circles indicate the peak inspiratory histogram and squares indicate the peak expiratory histogram. The image from 0 to 5 represents the expiration phase, and image from 5 to 9 represents the inspiration phase. HU: Hounsfield units.

requires manual registration of pulmonary regions, which is time consuming and prone to error. We previously described the use of the optical flow method (OFM), a deformable image registration algorithm, to register eBH-CT and iBH-CT image pairs, providing a tissue-motion map that links tissue elements between the image pairs (Guerrero *et al* 2004). We also described the generation of static 3D ventilation images from the eBH-CT and iBH-CT image pairs (Guerrero *et al* 2005). 4D CT images differ significantly from BH-CT images and are not routinely used in diagnostic evaluation. They contain residual respiratory-related motion resulting in non-uniform blurring of the image, discontinuities may arise along the superior–inferior axis because the images are acquired during different breaths, they have higher statistical noise content than BH-CT images because of efforts to reduce the dose to the patient and they result in an order of magnitude increase in the number of images. However, 4D CT images are acquired in the uniform physiological state of normal resting tidal breathing, and the resulting images reflect the dynamics of resting ventilation.

In this study, we developed a ventilation imaging method that requires no tracer and is performed using a multislice CT scanner on freely breathing resting patients from the same CT images acquired for radiotherapy treatment planning. We also demonstrate the generation of quantitatively accurate, temporally resolved dynamic ventilation images from 4D CT data and perform a simple validation with manually segmented lung parenchymal volumes. Finally, we evaluated the resulting 4D ventilation images with regard to specific ventilation along the major anatomical axes.

2. Materials and methods

2.1. Patients and CT data

Three patients who had been treated for lung cancer in the Department of Radiation Oncology at The University of Texas M D Anderson Cancer Center who received 4D CT imaging as

part of their treatment planning were selected from the patient database for this retrospective study. The patient identifiers were removed in accordance with the retrospective study protocol approved by our Institutional Review Board. Each patient had undergone a treatment planning session where a 4D CT image of the entire thorax and upper abdomen was obtained at 3 mm slice spacing on a PET/CT scanner (Discovery ST; GE Medical Systems, Waukesha, WI) with a 70 cm bore (figure 1). The images had been acquired with the patients in the supine position with normal resting breathing. The 4D CT acquisition technique using the respiratory signal from the real-time position management respiratory gating system (Varian Medical Systems, Palo Alto, CA) has been previously described (Pan *et al* 2004).

2.2. Deformable image registration

The goal of deformable image registration is to find a point-to-point voxel correspondence between two given images. This desired correspondence should relate the location of each underlying tissue element represented in each voxel in the first image to that in the second image. The OFMs (Horn and Schunck 1981) comprise a large class of image registration techniques that find such a correspondence by computing a velocity field describing the apparent motion depicted in the two images. For a single pair of images, the velocity field is equal to the displacement field with the time step assumed as unity. Several reviews of these methods exist, as do reports of studies that focused on the performance of different optical flow implementations and techniques (see Beauchemin and Barron (1995), for example).

Assume that the two given images are snapshots of an unknown brightness function:

$$I(x(t), t), \quad t \in [0, t_1], \quad x(t) \in \Omega, \quad (1)$$

where $\Omega \subset \mathbb{R}^3$ is the region of interest captured by the images. The brightness of any particular voxel is assumed to remain constant through time:

$$I(x(t), t) = \text{constant}. \quad (2)$$

Therefore, the total time derivative of the brightness function is zero. Applying the chain rule for differentiation to $I(x(t), t)$ yields the well-known optical flow equation:

$$\frac{dI}{dt} = \frac{\partial I}{\partial t} + \nabla I \cdot \mathbf{v} = 0, \quad (3)$$

where $\mathbf{v} \subset \mathbb{R}^3$ is the velocity vector to be determined at each point in Ω .

An additional ‘smoothness’ assumption, that neighbouring voxels move similarly relative to each other, is required to solve for the three unknown velocity components of \mathbf{v} . This assumption implies that the velocity field does not vary greatly in space. Consequently, the gradients of the velocity components v_i , $i = 1, 2, 3$, should be small. Both the brightness and smoothness assumptions are incorporated into a penalty function formulation. The velocity field is the solution to the following minimization problem:

$$\min \int_{\Omega} \alpha^2 \sum_{i=1}^3 \|\nabla v_i\|^2 + \left\| \frac{\partial I}{\partial t} + \nabla I \cdot \mathbf{v} \right\|^2 dx, \quad (4)$$

where α is a penalty parameter determining the amount of smoothness one wishes to incorporate. According to the calculus of variations, ‘optimality’ conditions for (4) are given, under suitable boundary conditions, by the following system of partial differential

equations:

$$\left(\frac{\partial I}{\partial t} + \nabla \cdot \mathbf{v}\right) \nabla I - \alpha^2 \begin{bmatrix} \nabla^2 v_1 \\ \nabla^2 v_2 \\ \nabla^2 v_3 \end{bmatrix} = 0, \quad (5)$$

where ∇^2 is the Laplacian operator.

The partial differential equations are discretized, resulting in a linear system of equations for the velocities at each voxel. This results in an iterative procedure to solve this linear system at each voxel:

$$\mathbf{v}_{n+1} = \overline{\mathbf{v}}_n + \nabla I \left(\frac{\nabla I \cdot \overline{\mathbf{v}}_n + \frac{\partial I}{\partial t}}{\alpha^2 + \|\nabla I\|^2} \right), \quad (6)$$

where n and $n + 1$ are iteration counts and $\overline{\mathbf{v}}_n$ is the average velocity taken over the nearest neighbouring voxels. This method is equivalent to a version of the well-known Gauss–Seidal method (Press *et al* 2002) when the latest available velocity values are used in calculating the average. The temporal and spatial derivatives in equation (6) are approximated with finite differences and applied to the two given images.

2.3. CT ventilation theory

The mapping of each voxel, or tissue element, between the eBH-CT and iBH-CT image sets allows for the identification of corresponding tissue elements. Since the mapping may contain some error, $3 \text{ mm} \times 3 \text{ mm} \times 3 \text{ mm}$ local averages of the CT HU for each eBH-CT voxel (HU_{ex}) and the mapped iBH-CT voxel (HU_{in}) are obtained. A mass correction, to correct for respiratory-induced changes in tissue perfusion (Brower *et al* 1985), is applied to the iBH-CT images (unpublished method).

Simon (2000) reported a relationship between manually registered CT regional values (HU_{ex} and HU_{in}) and the regional volume change. First, a correction is applied to each voxel in the inspiration image to account for the difference in CT-derived mass due to the changes in blood distribution between the two images:

$$\text{HU}_{\text{corrected}} = \text{HU}_{\text{uncorrected}} - 1000f \left(1 + \frac{\text{HU}_{\text{uncorrected}}}{1000} \right), \quad (7)$$

where f is the fractional discrepancy in total lung tissue mass between the expiration and inspiration CT images.

Simon's method assumes that the fraction of air in a CT region is given by

$$F_{\text{air}} = -\frac{\text{HU}}{1000}. \quad (8)$$

According to Simon (2000),

$$\frac{\Delta V}{V_{\text{ex}}} = \frac{F_2 - F_1}{F_1(1 - F_2)}, \quad (9)$$

where F_1 is the fraction of air in the expiration CT volume element and F_2 is the fraction of air in the inspiration CT volume element. Then

$$\frac{\Delta V}{V_{\text{ex}}} = \frac{F_{\text{ex}} - F_{\text{in}}}{F_{\text{ex}}(1 - F_{\text{in}})}. \quad (10)$$

Substitution from equation (8) yields

$$\frac{\Delta V}{V_{\text{ex}}} = 1000 \frac{HU_{\text{in}} - HU_{\text{ex}}}{HU_{\text{ex}}(1000 + HU_{\text{in}})}, \quad (11)$$

where $\Delta V = V_{\text{in}} - V_{\text{ex}}$ is the local volume change due to inspiration.

In our study, we applied equation (11) for all pulmonary voxels ($HU < -250$) contained in the segmented lung volumes to obtain a parametric image representing local fractional volume change ($\frac{\Delta V}{V_{\text{ex}}}$). Then we performed $9 \text{ mm} \times 9 \text{ mm} \times 9 \text{ mm}$ spatial averaging of the resulting (ventilation) parametric images to generate the final 3D ventilation image.

The minimum volume CT was phase 5 from the 4D CT data set. The following phases were paired to represent inspiration: 5 to 6, 5 to 7, 5 to 8, 5 to 9 and 5 to 0. The expiratory phases were represented by the following pairs: 5 to 1, 5 to 2, 5 to 3 and 5 to 4. The OFM algorithm was applied to these pairs of images to produce a mapping of each voxel in phase 5 to each of the other images. Ventilation images were generated from those mappings and equations (7) and (11). The phase 5 to phase 0, representing the tidal ventilation, was imported into the Pinnacle version 6.2b radiotherapy treatment planning system (Pinnacle³, Phillips Radiation Oncology Systems, Milpitas, CA). A region of interest which contained 30% of the total function and the highest ventilation values was generated utilizing the auto-segmentation option in Pinnacle and a cut-off value determined from histogram evaluation of the ventilation images.

2.4. Tidal volume validation

For each CT image pair used for ventilation calculation, we compared the computational method for determination of tidal volume with the volume change observed with manual delineation of the lungs. The lungs were segmented using an automated histogram segmentation tool available in the Pinnacle (version 6.2b) treatment planning system (Pinnacle³, Philips Radiation Oncology Systems, Milpitas, CA). The trachea and main-stem bronchi were excluded from the volume, as was the primary lung tumour volume. The difference in lung volume between the expiration and inspiration image volumes represented the measured tidal volume. The computational method for determination of change in lung volume, represented by equations (7) and (11), was the summation of the voxel ventilation values for all the pulmonary parenchyma. The total tidal volumes obtained by summing the ventilation image voxels were compared with the manually segmented lung volumes for each image pair with and without the mass correction. A linear equation, in which we expected one-to-one correspondence, was then fit to the data.

2.5. Dynamic ventilation distribution

The mass-specific ventilation (MSV) is defined here as the ventilation for a region divided by the parenchymal mass of the lung for that region. This is given by the following equation:

$$V_{\text{m}} = \frac{\Delta V}{\int_V \rho \, dV}, \quad (12)$$

where the density ρ is calculated from the CT values by

$$\rho = 1 + \frac{HU}{1000}. \quad (13)$$

The distribution of the MSV is calculated along the major anatomical axes (i.e. superior–inferior, posterior–anterior and medial–lateral) of each ventilation image by dividing the images into halves along each axis and comparing the halves. This technique reveals the

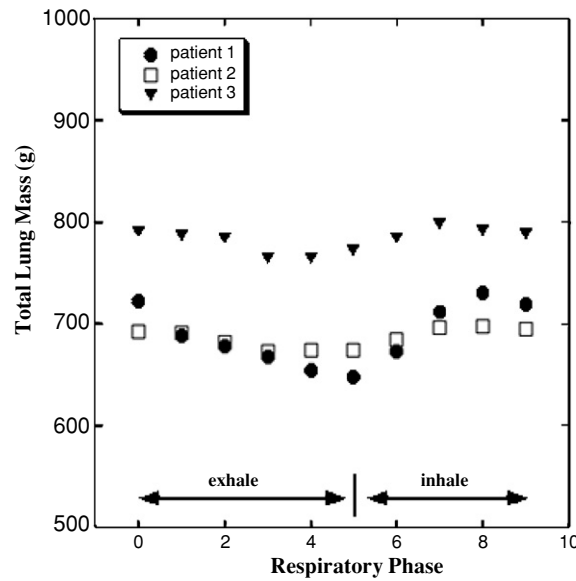


Figure 3. The total mass of the lung parenchyma ($HU < -250$) for each patient (patients 1–3) was calculated within the manual segmented lungs from the CT values and equation (13). Note that there are differences between the three patients' data in amplitude and average value.

dynamic distribution of ventilation throughout the respiratory cycle. An MSV profile is calculated for each ventilation image to illustrate the dynamic ventilation through the complete respiratory cycle.

3. Results

3.1. 4D CT image properties

Figure 1 shows a coronal image from the extreme inspiration and expiration phases from a typical 4D CT image set along with two labelled regions of interest (ROIs), one in the right lower lobe (ROI-1) and the other in the left apex (ROI-2). A graph of the lung volume versus the image phase (figure 2(a)) for one patient illustrates both the expiration and inspiration limbs of the respiratory cycle and revealed that the maximum volume occurred at image phase 0 and the minimum volume at image phase 5. In the histogram made from the segmented lungs for each CT image (figure 2(b)), the change in CT values over the respiratory phase is apparent: the end-inspiratory histogram contains the most negative CT value distribution, and the end-expiratory histogram contains the most positive distribution. The distribution of the remaining respiratory phases lies between these two extremes.

The pulmonary tissue histograms changed only for CT values < -250 HU (Guerrero *et al* 2005). The mass of the pulmonary parenchyma (CT values < -250 HU) was calculated for each CT image of each of the three patients (figure 3) from the local densities obtained using equation (13). We found a cyclic variation in the apparent mass of the pulmonary parenchyma: the mean value and the percentage of variation were different for each patient. This cyclic variation represents the changing perfusion in the pulmonary parenchyma that results from local mechanical factors, such as the distension of blood vessels, and from the variation in respiratory-induced cardiac output (Cournand 1957, Brower *et al* 1985).

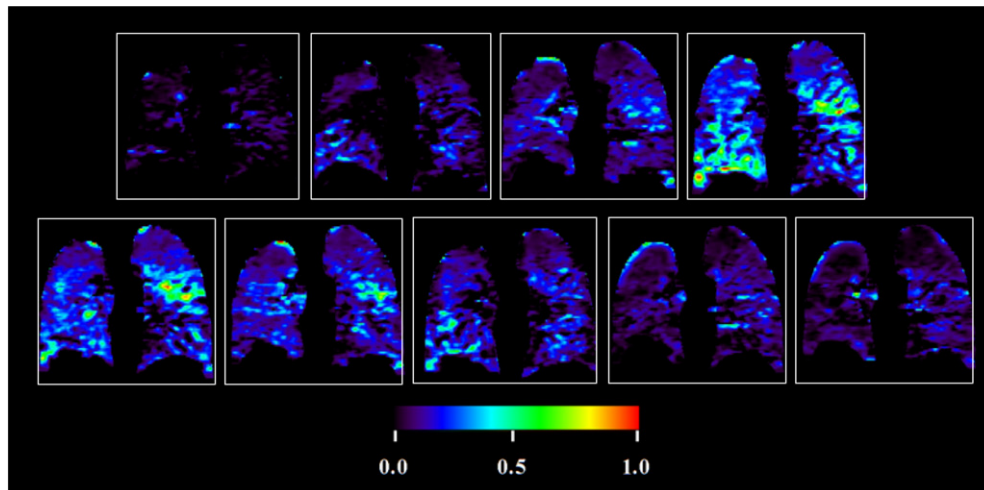


Figure 4. This figure illustrates the 4D CT ventilation image set of patient 1 (coronal sections). A pair of CT images was used for each ventilation image. Each image was paired with the maximum expiration images to calculate the difference in fraction of air with respect to the maximum expiration. The images from the top row represent inspiration and the bottom row represents expiration. The colour scale beneath the images represents the fractional increase in voxel volume; for example, a value of 0.5 represents a 50% increase in volume between the two corresponding voxels from the CT pair.

3.2. Dynamic ventilation and validation

For the image pairs formed with the maximum expiration image, ventilation images were calculated using equations (7) and (11). Mapping of each image pair was performed in the direction that allowed calculation of the ventilation image onto the image that had the larger lung volume; this incorporated the respiratory motion into the dynamic ventilation image set as well. If the mapping was performed in the opposite direction, the resulting ventilation images would have a constant anatomical reference frame, that of the maximum expiration image. Figure 4 shows a coronal section from one patient (number 1), where the value of each voxel represents the fractional percentage increase in volume. The resulting ventilation images had few negative values. The total change in lung volume was obtained by summing the product of the voxel volume with the value of each voxel from the ventilation image.

We then compared the fractional increase in total lung volume obtained from the ventilation images with the fractional volume change determined by the manually measured segmented lung volumes (figure 5(a)) for each patient. The first comparison made was of the ventilation images obtained without using the mass correction. Linear regression analysis resulted in a slope of 0.453, a correlation coefficient value of $r = 0.946$ and a non-zero offset of 0.063 ml. These findings of a non-unity slope and non-zero offset suggested the presence of a systematic error. Our second comparison, using the mass-corrected ventilation images, resulted in a linear regression slope of 1.00, a correlation coefficient value of $r = 0.985$ and an offset of 0.040 ml. The offset represents a small, stable systematic error over the 27 volume pairs from the images of our three patients evaluated. Thus, the use of the mass correction resulted in better correlation between the calculated ventilation images and the measured changes in lung volume than that obtained without the use of the mass correction. In addition, we calculated the absolute total ventilation in ml of air and compared it with the measured change in absolute volume; linear regression analysis resulted in a slope of 1.01, a correlation

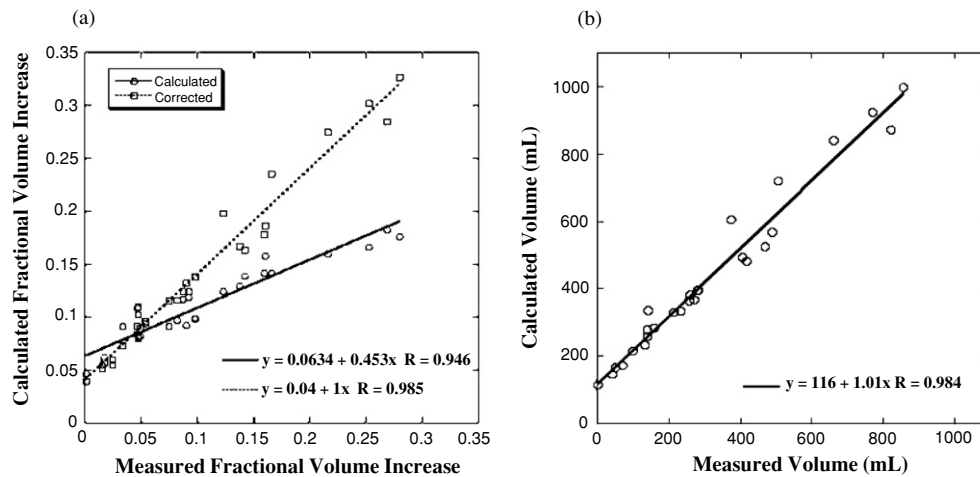


Figure 5. Correlation of calculated with measured tidal volumes. (a) The fractional increase in total lung volume from each pair of images from all three patients (27 CT pairs) was obtained by both calculation and direct measurement. Both uncorrected and mass-corrected calculated values are shown. Linear regression analysis resulted in a slope of 1.0001 and a correlation coefficient of $r = 0.985$ for the mass-corrected values. (b) The absolute tidal volumes were calculated from the fractional values and plotted against the measured absolute volumes. The resulting slope of 1.01 and correlation coefficient of $r = 0.984$ represent good correlation.

value of $r = 0.984$ and an offset of 116 ml. Finally, the calculated tidal volumes correlated well with the measured tidal volumes.

The maximum ventilation image from one case (patient 3) was imported into a treatment planning system. Based on histogram evaluation of the image values, a cut-off point corresponding to the top twelve percentile of the ventilation values was found. A region of interest was generated utilizing the auto-contouring tools available in the treatment planning system, as shown in figure 6, where the lung function defined region is shown in green and the planning target volume is shown in red. The preponderance of the high functional density region is located in the lower half of the lung.

3.3. Dynamic ventilation distribution

Using equation (12), we calculated the MSV value for each z position along the superior–inferior axis in each of the component ventilation images, forming profiles of the MSV along the z -axis (figure 7(a)). The resulting distribution of the specific ventilation was non-uniform and changed with the respiratory phase. For each of the three patients, we also calculated the MSV value for each half of the lung volume divided along the superior–inferior axis; the resulting values, again plotted against the respiratory phase, appear in figure 7(b). In patient 1, the superior half–inferior half ratio changed with the respiratory phase: the maximum difference in MSV occurred at the earliest expiration phase, and the minimum difference at the end-expiration phase. The variation in MSV between the two halves of the lung was less pronounced in the other two patients. The largest MSV value in any patient approached 1 ml of air per gram of lung tissue. We then calculated the MSV for the volume of each half lung divided along each of the three anatomical axes and calculated the ratios between each pair of those halves. The average values of those ratios across the respiratory cycle in each patient are given in table 1 for each axis. The ratio between the superior and inferior halves reveals

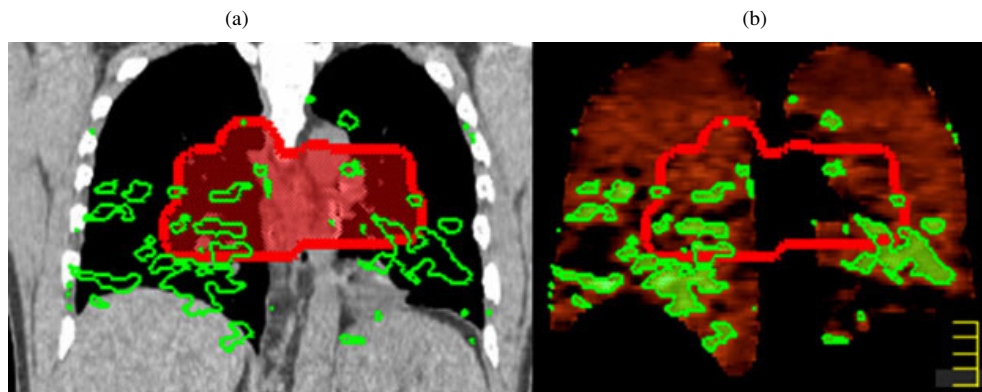


Figure 6. The tidal ventilation image volume, corresponding with the ventilation calculated from phase 5 to phase 0, of patient 3 was imported into the Pinnacle version 6.2b radiation therapy treatment planning system (Pinnacle³, Phillips Radiation Oncology Systems, Milpitas, CA). A region of interest which contained the top twelve percentile of ventilation values was generated utilizing the auto-segmentation option in Pinnacle. (a) A coronal section through the treatment planning CT is shown with the planning target volume (PTV) outlined in red and the lung function defined region in green. (b) The corresponding coronal section through the ventilation image is shown also with the PTV in red and the lung function defined region in green.

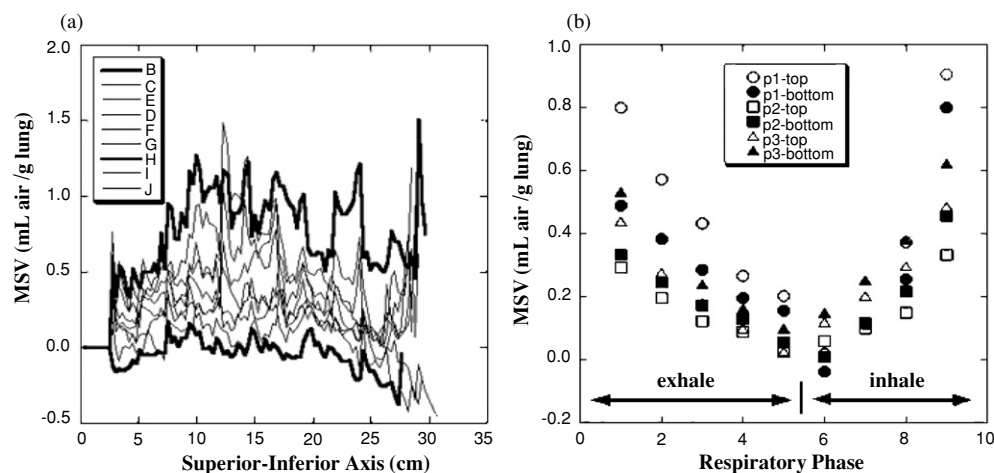


Figure 7. The regional distribution of mass-specific ventilation (MSV) was evaluated versus the phase of the respiratory cycle. (a) Profiles of the MSV along the superior–inferior axis. Note that each curve has a considerable amount of modulation. (b) The ventilation images were bisected along the superior–inferior axis, and the MSV was obtained for each half (top and bottom) of the lung for each patient. The relative changes in the MSV values over the course of the respiratory cycle are indicated in the graph.

that patient 1 had higher MSV in the superior half of the lung whereas the other two patients had the MSV higher in the lower half of the lung. Radiation injury to the half of the lung with the higher MSV will result in 30% more loss of function per gram of lung tissue injured than would an injury to the other half of the lung (which has the lower MSV). Knowledge of these values in individual patients may be useful in radiotherapy treatment planning to minimize loss of pulmonary function following radiotherapy.

Table 1. Ratios of mass-specific ventilation (MSV) for three patients. The MSV was calculated for the volume of each half of the lung along each of three axes.

Patient	Position of primary tumour	MSV ratio for each axis		
		Superior–inferior	Right–left	Anterior–posterior
1	Left lower lobe	1.36	1.18	1.07
2	Mediastinum	0.727	1.17	1.06
3	Right lower lobe	0.703	1.07	1.19

4. Discussion

To our knowledge, this report is the first to describe the calculation of dynamic ventilation images from contrast-free 4D CT. As our results indicated, this new technique is potentially an improvement over the methods currently used for ventilation imaging. For example, a pre-surgical or pre-radiotherapy pulmonary evaluation may involve both resting and stress tests to indicate both the loss of function at rest after resection or radiotherapy and the reserve that will be available to the patient to compensate for that loss of function. Because our new method does not require the administration of a radioactive compound or tracer, as the established methods do, repeat testing, such as a stress ventilation test, could be performed immediately after the resting test in the same setting. However, the dose to the patient for 4D CT is higher than from a tracer-based ventilation study. 4D CT imaging is used routinely in thoracic radiotherapy treatment planning and the calculation of a ventilation image adds no additional dose to the patient. In this study, we found that the ventilation distribution changed with the respiratory phase, which indicates that the underlying ventilation reserve may not be simply proportional to the resting function. The images that result are registered with the underlying CT images allowing detailed evaluation of the pulmonary anatomy as well as calculation of the underlying lung mass and the resulting MSV. For the non-radiotherapy patient, the potential benefits of improved anatomical information over existing ventilation imaging may justify the additional dose compared with current radioactive tracer-based ventilation imaging methods. Further evaluation of the clinical role for this method is required.

The resolution and properties of the ventilation images generated in this study have yet to be evaluated, their resolution may be only limited by the CT scanner's resolution capability and the spatial accuracy of the deformable image registration algorithm. It is known that optical flow performs well when the voxel displacements are relatively small and the image is relatively smooth (Beauchemin and Barron 1995), though a number of factors can affect the quality of registration. To the best of our knowledge, there are no theoretical, quantitative error estimates available today for this methodology. Empirical and experimental verifications are still the only practical validation techniques to estimate the registration error. We have found the displacement errors for a phantom tumour to be within one voxel dimension, for the ideal case where the image is shifted (Guerrero *et al* 2004). The uncertainty in positioning for 4D CT images is greater. To account for this uncertainty, local 3 mm³ averages are used when sampling the CT images as discussed in section 2. In addition, the final resulting image was smoothed using a 9 mm³ average box filter. The resulting dynamic ventilation image set was validated using the anatomic whole lung volumes obtained through segmentation of the component CT images. The dynamic ventilation produced in this study is a 4D representation of normal supine resting breathing and provides an accurate quantitative estimate of absolute ventilation in that physiological state. The distribution of ventilation revealed in our patients was non-uniform, but the CT images we utilized were acquired in these patients because each

was a candidate for radiotherapy of their lung cancer. Only the 4D CT images were utilized in the treatment planning for these patients at the time the images were obtained, but the ventilation images we can now obtain using this new method could readily be incorporated into the planning process. Hence, the functional heterogeneity of the lungs could be taken into account during the treatment planning and evaluation. For example, an avoidance structure may be generated from the most active lung regions (figure 6) and utilized in treatment plan optimization.

In current radiotherapy treatment planning, the risk of pulmonary injury (Graham *et al* 1999, Lee *et al* 2003) is calculated assuming a homogeneous pulmonary function throughout the entire lung (Lyman 1985). However, we have found that patients may have significantly heterogeneous spatial distributions of lung function. For example, in this study a difference of 30% was found between the upper and lower lung halves in some cases. A more accurate method of risk assessment would include both the volume and the functional capacity of the portions of the lung targeted for irradiation (Marks *et al* 1995, Nioutsikou *et al* 2005). Marks *et al* (1997) proposed the use of 3D lung perfusion imaging as a marker for regional pulmonary toxicity in patients treated with radiation; they and others reported that a dose-dependent reduction in pulmonary perfusion occurred after irradiation of the lung (Marks *et al* 1997, Theuws *et al* 1998). A linear dose-dependent decrease in pulmonary ventilation has also been demonstrated in irradiated lung tissue (Theuws *et al* 1998). Assuming that a linear relationship exists between ventilation and pulmonary function, a biological index such as the mean ventilation-weighted lung dose may be useful in radiotherapy treatment plan evaluation; the development of such an index would parallel that of the mean perfusion-weighted lung dose proposed by Nioutsikou (Nioutsikou *et al* 2005). However, further research is needed to determine whether the use of the ventilation imaging developed in this study can fill that role.

A more extensive study to compare our newly developed dynamic ventilation imaging method with the existing methods will be necessary to complete its evaluation before we begin using it routinely in the clinic.

5. Conclusions

In this study, a new methodology for imaging regional ventilation is introduced and validated: the calculation of dynamic regional ventilation images from 4D CT images. 4D CT images acquired for radiotherapy treatment planning contain both tumour motion and regional ventilation content; we have shown that the ventilation content may be extracted for explicit use. These pulmonary functional images may be useful in normal tissue avoidance in radiotherapy treatment planning or as a diagnostic evaluation of regional ventilation where both physiological and quantitative values are required for longitudinal studies.

Acknowledgments

We most sincerely thank the Department of Computational and Applied Mathematics at Rice University for providing an informal series of seminars on applied computational methods in medicine, funded through a National Science Foundation VIGRE grant (NSF DSM 0240058). We also extend our warmest gratitude to Dr Elizabeth Travis, who organized The University of Texas M D Anderson Cancer Center's multi-disciplinary research project 'Lung Injury Following Cancer Treatment', which provided both motivation and funding for this project. Additional funding was provided through The University of Texas M D Anderson Cancer Center's Physician-Scientist Training Program.

References

- Albert M S, Cates G D, Driehuys B, Happer W, Saam B, Springer C S Jr and Wishnia A 1994 Biological magnetic resonance imaging using laser-polarized ^{129}Xe *Nature* **370** 199–201
- Alderson P O and Line B R 1980 Scintigraphic evaluation of regional pulmonary ventilation *Semin. Nucl. Med.* **10** 219–42
- Altemeier W A, McKinney S and Glenny R W 2000 Fractal nature of regional ventilation distribution *J. Appl. Physiol.* **88** 1551–7
- Altes T A and Salerno M 2004 Hyperpolarized gas MR imaging of the lung *J. Thorac. Imaging* **19** 250–8
- Beauchemin S S and Barron J L 1995 The computation of optical flow *ACM Comput. Surv.* **27** 433–66
- Brower R, Wise R A, Hassapoyannes C, Bromberger-Barnea B and Permutt S 1985 Effect of lung inflation on lung blood volume and pulmonary venous flow *J. Appl. Physiol.* **58** 954–63
- Burch W M, Sullivan P J and McLaren C J 1986 Technegas—a new ventilation agent for lung scanning *Nucl. Med. Commun.* **7** 865–71
- Cournand A 1957 Pulmonary circulation: its control in man, with some remarks on methodology *Science* **125** 1231–5
- Edelman R R, Hatabu H, Tadamura E, Li W and Prasad P V 1996 Noninvasive assessment of regional ventilation in the human lung using oxygen-enhanced magnetic resonance imaging *Nat. Med.* **2** 1236–9
- Fan M, Marks L B, Hollis D, Bentel G G, Anscher M S, Sibley G, Coleman R E, Jaszczak R J and Munley M T 2001 Can we predict radiation-induced changes in pulmonary function based on the sum of predicted regional dysfunction? *J. Clin. Oncol.* **19** 543–50
- Ford E C, Mageras G S, Yorke E and Ling C C 2003 Respiration-correlated spiral CT: a method of measuring respiratory-induced anatomic motion for radiation treatment planning *Med. Phys.* **30** 88–97
- Glenny R W, Bernard S L and Robertson H T 2000 Pulmonary blood flow remains fractal down to the level of gas exchange *J. Appl. Physiol.* **89** 742–8
- Graham M V, Purdy J A, Emami B, Harms W, Bosch W, Lockett M A and Perez C A 1999 Clinical dose–volume histogram analysis for pneumonitis after 3D treatment for non-small cell lung cancer (NSCLC) *Int. J. Radiat. Oncol. Biol. Phys.* **45** 323–9 (see comment)
- Guerrero T M, Sanders K, Noyola-Martinez J, Castillo E, Zhang Y, Tapia R, Guerra R, Borghero Y and Komaki R 2005 Quantification of regional ventilation from treatment planning CT *Int. J. Radiat. Oncol. Biol. Phys.* **62** 630–4
- Guerrero T, Zhang G, Huang T C and Lin K P 2004 Intrathoracic tumour motion estimation from CT imaging using the 3D optical flow method *Phys. Med. Biol.* **49** 4147–61
- Horn B K P and Schunck B G 1981 Determining optical flow *Artif. Intell.* **17** 185–203
- Kauczor H U, Hanke A and Van Beek E J 2002 Assessment of lung ventilation by MR imaging: current status and future perspectives *Eur. Radiol.* **12** 1962–70
- Kuethe D O, Caprihan A, Gach H M, Lowe I J and Fukushima E 2000 Imaging obstructed ventilation with NMR using inert fluorinated gases *J. Appl. Physiol.* **88** 2279–86
- Kwa S L S, Theuvs J C M, van Herk M, Muller S H and Lebesque J V 1995 Application of chamfer matching in three-dimensional correlation of CT–SPECT and CT–CT of the lungs *Radiother. Oncol. (Suppl.)* **37** S3–67
- Lee H K *et al* 2003 Postoperative pulmonary complications after preoperative chemoradiation for esophageal carcinoma: correlation with pulmonary dose–volume histogram parameters *Int. J. Radiat. Oncol. Biol. Phys.* **57** 1317–22
- Lyman J T 1985 Complication probability as assessed from dose–volume histograms *Radiat. Res. (Suppl.)* **8** S13–9
- Mageras G S *et al* 2004 Measurement of lung tumor motion using respiration-correlated CT *Int. J. Radiat. Oncol. Biol. Phys.* **60** 933–41
- Marks L B, Munley M T, Spencer D P, Sherouse G W, Bentel G C, Hoppenworth J, Chew M, Jaszczak R J, Coleman R E and Prosnitz L R 1997 Quantification of radiation-induced regional lung injury with perfusion imaging *Int. J. Radiat. Oncol. Biol. Phys.* **38** 399–409
- Marks L B, Spencer D P, Sherouse G W, Bentel G, Clough R, Vann K, Jaszczak R, Coleman R E and Prosnitz L R 1995 The role of three-dimensional functional lung imaging in radiation treatment planning: the functional dose–volume histogram *Int. J. Radiat. Oncol. Biol. Phys.* **33** 65–75
- Nioutsikou E, Partridge M, Bedford J L and Webb S 2005 Prediction of radiation-induced normal tissue complications in radiotherapy using functional image data *Phys. Med. Biol.* **50** 1035–46
- Pan T 2005 Comparison of helical and cine acquisitions for 4D-CT imaging with multislice CT *Med. Phys.* **32** 627–34
- Pan T, Lee T Y, Rietzel E and Chen G T 2004 4D-CT imaging of a volume influenced by respiratory motion on multi-slice CT *Med. Phys.* **31** 333–40
- Press W H, Teukolsky S A, Vetterling W T and Flannery B P 2002 *Numerical Recipes in C++: The Art of Scientific Computing* (Cambridge: Cambridge University Press)
- Schuster D P 1998 The evaluation of lung function with PET *Semin. Nucl. Med.* **28** 341–51

- Simon B A 2000 Non-invasive imaging of regional lung function using x-ray computed tomography *J. Clin. Monit. Comput.* **16** 433–42
- Suga K 2002 Technical and analytical advances in pulmonary ventilation SPECT with xenon-133 gas and Tc-99m-Technegas *Ann. Nucl. Med.* **16** 303–10
- Suga K, Nishigauchi K, Kume N, Takano K, Koike S, Shimizu K and Matsunaga N 1997 Ventilation abnormalities in obstructive airways disorder: detection with pulmonary dynamic densitometry by means of spiral CT versus dynamic Xe-133 SPECT *Radiology* **202** 855–62
- Tajik J K, Chon D, Won C, Tran B Q and Hoffman E A 2002 Subsecond multisection CT of regional pulmonary ventilation *Acad. Radiol.* **9** 130–46 (see comment)
- Theuvs J C M, Kwa S L S, Wagenaar A C, Boersma L J, Damena E M F, Mullera S H, Baas P and Lebesque J V 1998 Dose-effect relations for early local pulmonary injury after irradiation for malignant lymphoma and breast cancer *Radiother. Oncol.* **48** 33–43
- Underberg R W, Lagerwaard F J, Cuijpers J P, Slotman B J, van Sornsen de Koste J R and Senan S 2004 Four-dimensional CT scans for treatment planning in stereotactic radiotherapy for stage I lung cancer *Int. J. Radiat. Oncol. Biol. Phys.* **60** 1283–90
- Vedam S S, Keall P J, Kini V R, Mostafavi H, Shukla H P and Mohan R 2003 Acquiring a four-dimensional computed tomography dataset using an external respiratory signal *Phys. Med. Biol.* **48** 45–62
- Venegas J G and Galletti G G 2000 Low-pass filtering, a new method of fractal analysis: application to PET images of pulmonary blood flow *J. Appl. Physiol.* **88** 1365–73